Photo-activated emitting defects in the Ce-doped CaSnF6 fluoride

Ines Andron, Christine Frayret, Manuel Gaudon, Alexandre Fargues, Etienne Durand, Mathieu Duttine, Olivier Toulemonde, Veronique Jubera

Photo- activated emitting defects in the Ce-doped $CaSnF_6$ fluoride

Ines Andron[1], Christine Frayret[2], Manuel Gaudon[1], Alexandre Fargues[1], Etienne Durand[1], Mathieu Duttine[1], Olivier Toulemonde[1], Véronique Jubera[1*]

[†] CNRS, Univ. Bordeaux, Bordeaux INP, ICMCB, UMR 5026, F-33600 Pessac, France

[‡] Laboratoire de Réactivité et de Chimie des Solides (LRCS), CNRS UMR 7314, Université de Picardie Jules Verne, 80039 Amiens, Cedex 1, France

*Corresponding authors: veronique.jubera@u-bordeaux.fr

KEYWORDS. Fluorides, DFT, Luminescence, Rare-earth, Stannate

ABSTRACT:

Considering the interest to develop new photochromic compounds, the Ce doped-$CaSnF_6$ have been selected and thoroughly characterized. After optimization of the synthesis route, the structural and morphological properties, are described. The origin of the optical properties and photochromic are supported by magnetic, RPE, ^{119}Sn Mossbauer, ^{19}F and ^{1}H MAS NMR characterizations. In addition to the UV luminescence of Ce^{3+} ions in the stannate compound, they revealed the impact point defects at the origin of an additional visible contribution to the global signal. In view of elucidating the relationships between the observed photochromism and the possible nature of these defects, experimental interpretations are discussed on the basis of a computational approach.

1- Introduction.

Photochromism of inorganic materials is of a high interest because in link with potential application for storage devices [1-3], molecule detection [4;5], radiation dosimeter [6;7] or security ink [8]. However, such application requires a fast switch and a significant color (emissive) contrast between two stable states in order to insure the dynamics and precision of the system. Even if bistable inorganic compounds involving an ability to be switched from one first state to a second one are known to exhibit their two different

states as stable regarding time, this property is not so common in literature. Reviewing this research area demonstrates that photochromoluminescent inorganic fluorides able to reversibly switch between two states with different emission spectrum under ultraviolet (UV)-light irradiation represent a family well suited to design the next generation of photo-switchable optical sensors. One can quote for instance Sizova et al. [9] who reported preliminary works on alkaline-earth fluorides. A few years ago Chaminade et al. investigated an elpasolite of formula Rb_2KInF_6:Ce [10]. This double perovskite compound is highly sensitive to the UV irradiation. Indeed, a redox process between Ce^{4+}/Ce^{3+} and In^{3+}/In^{+} ions results in an unexpected color change of the global emission. We have proposed in recent publications that the reason of such phenomenon could lie in the potential overlap between the t_{2g} 5d orbitals of Ce^{3+} located as substitution element into the In^{3+} octahedral sites with the 5s orbital of In^{3+} ions located as first neighbors of the Ce^{3+} ions [11]. The oxidation of two Ce^{3+} ions into two Ce^{4+} ions under UV is coupled with the trapping of the released electrons by In^{3+} which is by consequence reduced at the monovalent oxidation state.

Similarly to Rb_2KInF_6, $CaSnF_6$ exhibits a cubic unit cell, which can be described as a double ReO_3 structural-type. The crystallographic network is built on the alternation between Ca^{2+} and Sn^{4+} octahedra, with an edge-sharing pattern, i.e. a similar skeleton than in elpasolite structural-type [12;13]. In addition, the cost of the tin reactants and the tin resource availability represents a real advantage of this matrix composition compared to the indium-based elpasolite counterpart. Furthermore, the steric constraints of the tin site are compatible with its substitution by cerium ions.

We propose here to synthesize and fully characterize a Ce-doped $CaSnF_6$ matrix. Structural as well as optical, magnetic, and spectroscopic properties are thoroughly examined to investigate the potentiality of this compound as photochromic sensor. In view of interpreting the photochromism features and to search for an origin of the mechanism occurring during the optical process, a DFT investigation involving various configurations of the point defects suspected to be present from experimental observations is performed.

2-Materials and method

2.1 Syntheses.

Ce-doped $CaSnF_6$ was obtained by specific heat treatment of the Ce doped-$CaSn(OH)_6$ hydroxide. The first steps of the synthesis route are described in [13]. A longer maturation of the hydroxide before heat treatment was applied (2h at 55°C instead of 30 minutes at ambient temperature). In complement, heat-treatment in air was performed to stabilize the Ce-doped $CaSnO_3$ compound, as a potential impurity of the previous reaction. A solid-state synthesis route was also performed for comparison of the optical properties. Thus, CaF_2, SnF_3 and CeF_3 reactants were introduced in stoichiometric proportions, in a platinum tube sealed under Argon atmosphere. The tube has been heated at 800°C for 20h.

ii) Powder X-ray diffraction patterns were collected on a Philips X'Pert MPD X-ray diffractometer with a Bragg-Brentano geometry using Cu $K\alpha_{1,2}$ radiation ($10 < 2\theta < 130°$, step 0.02° and counting time of 30 s). Some of the diffractograms were refined using the pattern matching method with the conventional reliability factors. The Fullprof program package was used. Unit cell parameters, zero-shift and peak profile's parameters were refined.

2.2 ICP-OES titration

ICP/OES (Inductively Coupled Plasma / Optical Emission Spectrometry) was conducted on Varian ICP/OES 720 ES apparatus equipped with an Argon plasma torch and a CDD detector.

A Total dissolution of the products were performed in 7%HNO_3 (63%)/2%HCl (34-37%) acid.

2.3 SEM images

Photographs from scanning microscopes are also collected. The scanning electronic microscopy (SEM) analysis was made with a JEOL Field Emissive Gun - Scanning Electronic Microscope (FEG-SEM) in order to characterize the crystallite morphology (shape, size and special rearrangement) through a spatial resolution of about 1 nm.

2.4 Photoluminescent and kinetic analysis

The photoluminescent properties were analyzed using a Fluo3 Horiba spectrofluorimeter connected by a 450W continuous Xenon source. Raw data were corrected for the experimental parameters: variation of the incident flux, monochromator transmission and photomultiplier sensitivity. Decay time measurements were performed with an Edinburgh Instruments FL900CDT spectrofluorometer using a hydrogen flash lamp delivering subnanoseconds optical pulses. The decays were obtained by the time correlated single photon technique. Irradiation of the samples have been performed within the same equipment. The global power at the surface of the powder was equal to 220 W/m². This power was measure on an Agilent Avaspec ULS4096CL-Evo equipment.

2.5 Magnetism

A static magnetic flux (DC) with a MPMS-5S SQUID(Superconducting Quantum Interference Device) apparatus was used for the measurements which were performed between 2 and 100 K in an applied field ranging within the 0T-5T range in a zero-field-cooled process.

Data collected at 100 K were fitted to extract the diamagnetic contribution from the sample holder and $CaSnF_6$ host.

2.6 Mössbauer spectroscopy

^{119}Sn Mössbauer measurements were carried out using a constant-acceleration Halder-type spectrometer operating in transmission geometry with a room temperature $^{119\,m}$Sn source (370 MBq, $CaSnO_3$ matrix). Thin absorbers were prepared in order to contain about 10 mg.cm^{-2} of Sn (^{119}Sn natural abundance 8.59%). Mössbauer spectra were recorded at room temperature and the hyperfine parameters (δ isomer shift, Δ quadrupole splitting, Γ Lorentzian linewidth and relative areas) were refined using both homemade programs and the WinNormos® software (Wissenschaftliche Elektronik GmbH). The ^{119}Sn isomer shifts are referenced to $CaSnO_3$ at room temperature.

2.7 Solid-State Nuclear Magnetic Resonance (NMR) analysis

^{19}F and ^{1}H NMR experiments were performed with two Bruker spectrometers, an Avance III 100WB operating at 94.2 MHz for ^{19}F and an Avance III 300WB operating at 300.2 MHz for ^{1}H. Spectra were

recorded at Magic-Angle Spinning (MAS) rate of 30 kHz using a Hahn echo ($\pi/2$ - π) pulse sequence synchronized to one rotation period (33.33 μs) with a 2.0 μs ($\pi/2$) pulse and optimized recycle delays (from 5 to 60 s). Trifluorotoluene and Adamantane were used as secondary references, $\delta(^{19}F)$ = -63.9 ppm and $\delta(^{1}H)$ = +1.91 ppm, respectively.

2.8 Computational procedure:

All the calculations of undoped and Ce^{3+}-doped $CaSnF_6$ materials were performed within the density functional theory using the Vienna Ab initio simulation package (VASP) [14] and were carried out to optimize the cell parameters along with the positions of the atoms by considering 2×2×2 supercells (256 atoms if defect-free (*i.e.* for the undoped matrix)). The projector-augmented wave method (PAW) [15] and the PBE revised for solids GGA-PBEsol [16], as an approximation to the exchange-correlation functional, were used throughout. The valence wavefunctions were expanded in a plane-wave basis with a cut-off energy of 600 eV. A 2×2×2 grid was used for the k-point sampling of Brillouin zone. Feynman-Hellmann forces were minimized to be below 0.01 eV/Å in all structural relaxation calculations. When performing VASP-PAW calculations with the PBEsol exchange-correlation functional, the structural parameter of the undoped $CaSnF_6$ host crystal structure (space group Fm-3m) was found to be quite reasonable: a = 8.433 Å against a = 8.341 Å for the experimental value (with a relative error of 1.1%). All relative errors with respect to experimental structural features of pure $CaSnF_6$ were found to be improved compared to the PBE functional (see section 4).

3- Experimental results and discussion

3.1 Structural, morphological and chemical analyses.

Diffractograms of the powders resulting from the different syntheses routes are illustrated in Figure 1.

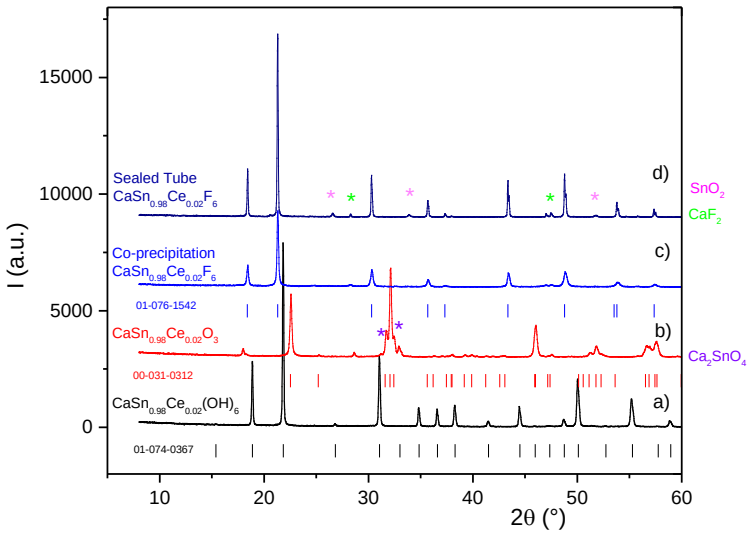

Figure 1: X-ray diffraction patterns of Ce-doped $CaSn(OH)_6$ compound (a), Ce-doped $CaSnO_3$ (b), Ce-doped $CaSnF_6$, hydroxide route (CP) (c), Ce-doped $CaSnF_6$, sealed tube route (ST) (d).

The three compounds crystallize into a cubic cell with the *P n −3 m, P b n m* and *F m − 3 m* space groups for $CaSn(OH)_6$, $CaSnO_3$ and $CaSnF_6$, respectively. NaCl phase appears as an impurity after the co-precipitation step leading to the formation of the hydroxide but it was easily washed in distilled water before the heat-treatments. A calcination under air leads to the stabilization of Ca_2SnO_4 and fluorine-type, with probably $(Ce,Sn)O_2$-based composition traces in addition to the $CaSnO_3$ main compound, but a direct heat-treatment at 200°C under HF makes possible the obtaining of nearly pure Ce-doped $CaSnF_6$ fluoride (CaF_2 trace) which is labelled CP. The fluoride compound synthesis through the sealed tube method is also reported in Figure 1 for comparison. It will be cited as ST sample. Traces of CaF_2 and SnO_2 are detected. The weaker width of the diffraction peaks shows a better crystallinity resulting from the solid-state route in comparison with the co-precipitation route.

Rietveld refinements have been performed on the CP fluoride compound taking into account several hypotheses. The successive steps to validate this model are illustrated in Figure SI1. The best results gathering experimental diffraction pattern, calculated one and differential signal are illustrated in Figure 2. The corresponding *a* cell parameter is equal to 8.338(3)Å. In such refinement, Ca^{2+} and Sn^{4+} cations atomic coordinates are equal to 0 0 0 (4a Wyckoff position) and 0.5 0.5 0.5 (*4b* Wyckoff position), respectively. F^- anion is located on *24e* position with the 0.264(1) 0 0 coordinates. Refinement process

has been made taking into account cationic partial disorder on the calcium and tin sites. The best reliability factors converged to values equal to *Rp*= 11.4, *Chi²*= 4.86 and *R-Bragg factor* of 4.46. This model corresponds to a location of 4.8% of tin at the calcium site and reversely.

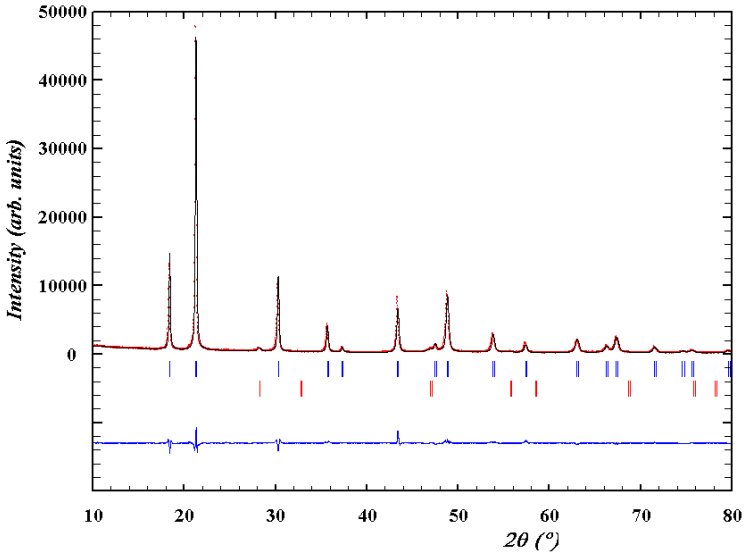

Figure 2: Rietveld type refinement of $CaSnF_6$ matrix (experimental point, I_{exp}: black circles; calculated curve I_{calc}: red line; $I_{exp} - I_{calc}$ difference: blue curve; theoretical position of $CaSnF_6$ diffraction peaks: blue scatter; theoretical position of CaF_2 diffraction peaks: red scatter)

The SEM pictures of Figure 3 highlight the hydroxide crystallization: because of a longer maturation time in this study compared with our previous work [13], a regular cubic morphology for the hydroxide is obtained. The observation of such regularly facetted cubes with very low rough surfaces for the $CaSnOH_6$ shows that each cube is monocrystalline. For the $CaSnO_3$ oxide and $CaSnF_6$ fluorides obtained respectively by air or HF annealing treatments, the double-hydroxide cubic crystallites act like templates during the germination-growth of the filiation compounds. Indeed, the cubic form is preserved under air heat treatment even if the formation of $CaSnO_3$ induces creation of porosity resulting from the departure of hydroxyl groups and an increase of the density from 3.20 $g.cm^{-3}$ for the $CaSn(OH)_6$ double hydroxide to 5.60 $g.cm^{-3}$ for the $CaSnO_3$ perovskite. After the heat-treatment under HF gas leading to the formation of $CaSnF_6$ compound, the cubic morphology is also maintained for the as-obtained aggregates. The

crystallite growth under HF results into denser polycrystalline grains, ingood agreement with the quite similar densities observed for the double hydroxide and the double fluoride (3.12 $g.cm^{-3}$) compounds.

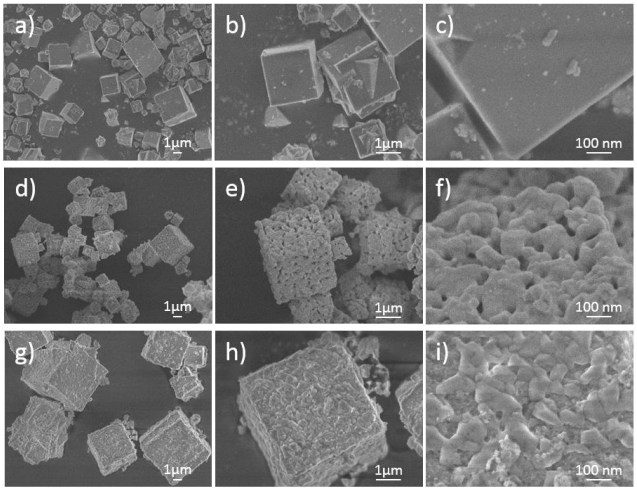

Figure 3: SEM pictures of Ce-doped $CaSn(OH)_6$ compound (a-c), Ce-doped $CaSnO_3$ (d-f), Ce-doped $CaSnF_6$ (hydroxide route) (g-h)

The partial substitution of Sn with Ce during the co-precipitation step with target compositions of $CaSn_{0.98}Ce_{0.02}(OH)_6$ was checked by ICP titration before going further into the characterizations. The molar proportion was normalized to obtain one mole of calcium per chemical formula. Table 1 indicates that the cerium content is consistent with the target compositions. However, it indicates a lack of tin, regarding the Sn:Ca experimental ratio expected for target compositions, with an average value being slightly lower than the desired ratio. This relative excess of calcium in the starting hydroxide is without any doubt the cause of the calcium-rich impurities such as Ca_2SnO_4 in addition to $CaSnO_3$ after the air treatment or such as CaF_2 besides $CaSnF_6$ after the HF treatment. During the co-precipitation process used to prepare the Ce-doped $CaSn(OH)_6$ hydroxide, because of different solubility for calcium and tin salts, the final incorporation yield inside the final precipitate is not exactly the same for the two ions. Although the double hydroxide network apparently accommodates a slight mismatch between the calcium and tin concentrations, the lack of calcium:tin stoichiometry results in the formation of calcium-rich secondary phases during mixed oxide or fluoride preparation.

Table 1. ICP titration results

Sample (targeted compo.)	**Ca (%weight)**	**Sn (% weight)**	**Ce (% weight)**	**Exp. Composition ***
$CaSn_{0.98}Ce_{0.02}(OH)_6$	15.7	41.3	1.3	$CaSn_{0.889}Ce_{0.024}(OH)_x$
$CaSn_{0.98}Ce_{0.02}O_3$	20.1	53.8	1.7	$CaSn_{0.903}Ce_{0.024}O_x$
$CaSn_{0.98}Ce_{0.02}F_6$	12.4	36.1	1.1	$CaSn_{0.983}Ce_{0.025}F_x$

3.2 Magnetic measurements: Ce^{3+} concentration

Magnetic measurements were also performed on CP. The interest of such characterization lying in the fact that the Ce^{3+} ions are the only paramagnetic species while Ce^{4+}, Sn^{4+}, Sn^{2+}, Ca^{2+} and F^- ions are all diamagnetic. Hence, magnetic measurements can be used to quantify the Ce^{3+}/Ce^{4+}concentration ratio in the studied compound. The Ce^{3+} Landé parameter (g) can be extracted considering L-S coupling such as g = 1+[((J|J+1|+S|S+1|)-L|L+1)/(2J|J+1|)] = 0.857 = 6/7 with S = ½ and L = 3 from the $4f^1$ electronic configuration. A first fit was performed considering only the x(Ce^{3+}) value as paramagnetic source. A second fit was performed refining the x(Ce^{3+}) value and an additional magnetic contribution, considered as originating from trapped electrons (latter, will be discussed the occurrence of trapped electrons on fluorine vacancies created consequently to the aliovalent substitution of Ce^{3+} for Sn^{4+} ions). With the magnetization in $J.K^{-1}.mol^{-1}$ and H in tesla, the magnetization curve for the first fit can be described by the following equation 1; for the second fit, magnetization follows the equation 2:

Equation 1 - $$M = 13.957 * x(Ce^{3+}) * g(Ce^{3+}) * \left[\frac{1.2}{\tanh(2.016*g(Ce^{3+})*H/T)} - \frac{0.2}{\tanh(0.336*g(Ce^{3+})*H/T)}\right]$$

Equation 2 - $$M = 13.957 * [Ce^{3+}] * g(Ce^{3+}) * \left[\frac{1.2}{\tanh(2.016*g(Ce^{3+})*H/T)} - \frac{0.2}{\tanh(0.336*g(Ce^{3+})*H/T)}\right] + 13.957 * x(e-) * g(e-) * \left[\frac{1.2}{\tanh(2.016*g(é)*H/T)} - \frac{0.2}{\tanh(0.336*g(é)*H/T)}\right]$$

The magnetization curves with additionally the two used fits is reported in Figure 4. The results are summed up in Table 2.

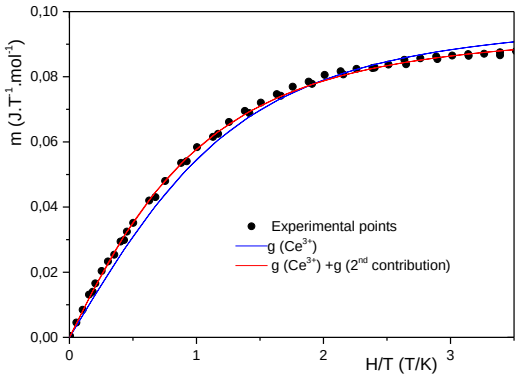

Figures 4- Magnetism characterization of Ce^{3+}-doped $CaSnF_6$ (CP)

Table 2- Results of the magnetic curve refinements

Parameters	Refinement results
$g(Ce^{3+})_{fixed}$	0.857
$x(Ce^{3+})$	0.008080
R^2	0.9634
$g(Ce^{3+})_{fixed}$	0.857
$x(Ce^{3+})$	0.006265
$g(2^{nd}\ contribution)_{fixed}$	2.0023
$x(2^{nd}\ contribution)$	0.000645
R^2	0.9884

First, it can be noted that from the fitting model the extracted concentration of Ce^{3+} in CP sample is calculated between 0.0062 and 0.0080. This clearly evidences that Ce^{3+} ions are in minor quantity compared with the Ce^{4+} ions, the Ce^{3+}/Ce^{4+} ratio being calculated between 0.3 and 0.45. The proportion of Ce^{4+} is therefore the majority in the $CaSnF_6$ host lattice. Hence, the occurrence of cerium (III) is demonstrated, proving that local defects (cations in interstitial sites or, more surely, anionic vacancies) should be present due to the charge compensation required to respect the electroneutrality of the system. The quality of the first fit is quite poor with an R^2 parameter equal to 0.96. However, taking into

account the additional magnetic contribution as minor impurity, a significant improvement of the correlation factor is observed: R^2 is now about 0.98. This contribution is ten times lower than that of Ce^{3+} ions but magnetic characterization highlights the need to consider these magnetic defects as a non-negligible contribution in the Ce^{3+} doped $CaSnF_6$ total signal. This second signal could be single electron trapped on a punctual defect as the anionic fluorine vacancy which should be created to compensate the charge deviation due to the introduction of the cerium at the trivalent oxidation state. It can be noted that, from magnetic measurement, the fluoride system can be viewed as a $CaSnF_6$ diamagnetic matrix with a mixture of $Ce^{3+}$and Ce^{4+} as doping ions with furthermore the possibility for Ce^{3+} to delocalize one electron in a neighboring electron trap (anionic vacancy).

3.3 Luminescence characterization of Ce-doped $CaSn(OH)_6$, $CaSnO_3$ and $CaSnF_6$ compounds.

Luminescence of trivalent cerium ion for the Ce-doped $CaSn(OH)_6$ and Ce-doped $CaSnO_3$ could not be detected even after reducing heat-treatment processes. This lack of radiative response in the hydroxide and oxide compounds can be explained first by the fact that cerium ions are stabilized with the +IV oxidation state. Secondly, a photoionization process could result in the promotion of the electron in the conduction band thus avoiding radiative recombination on the 5d orbitals of cerium, as it occurs in the case of the Ce^{3+}-La_2O_3 matrix [17]. Finally, the energy vibrations of the hydroxyl groups and/or surface defects can be strong enough to favor a total non-radiative de-excitation towards the ground state. However, the total lack of Ce^{3+} emission in the oxide is surprising since Borisevitch *et al.* have reported a blue-green emission for the Ce-doped $CaSnO_3$ host lattice [18]. The first blue contribution is due to radiative deexcitation from the lowest 5d orbital down to the $^2F_{5/2}$ and $^2F_{7/2}$ levels of Ce^{3+} ions. The second one is also linked to Ce doping process because an isovalent doping with La, Y or Lu does not result in any luminescence. But the origin of this large visible emission is not specifically attributed to a 5d-4f Ce^{3+} emission by the authors. Karabulut *et al.* also described a large green emission of Ce-doped $SrSnO_3$ [19]. This emission results from the convolution of several components which relative intensities depend on the excitation sources. These radiative transitions are said to be linked to “the presence of structural defects related to the incorporation of the large Ce^{3+} ion”. It thus discards a photoionization quenching process in the oxide compound and suggests that the thermal treatments applied is not sufficient to stabilize the Ce^{3+} ions in the matrix. This was confirmed by magnetic measurements performed on the

oxide powder which present a high diamagnetic contribution in agreement with the stabilization of Ce^{4+} ions (Figure SI2).

The luminescence of the two fluoride Ce-doped compounds is reported in Figure 5.

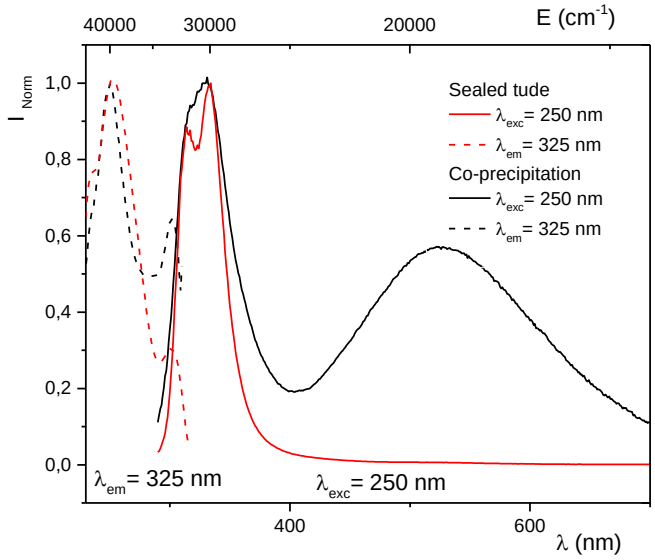

Figure 5: Normalized excitation and emission spectra of Ce-doped $CaSnF_6$ samples: co-precipitation route, *i.e.* CP sample (black curves); sealed tube synthesis ST sample (red curves).

The emission of the co-precipitation route compound (CP sample) presents two main contributions peaking at 315 nm and 335 nm separated by about 18950 cm^{-1}. These UV bands are due to the radiative de-excitation from the T_{2g} excited state of trivalent cerium ions down to the $^2F_{7/2}$ and $^2F_{5/2}$ levels. The maximum of the excitation spectrum points at 250 nm. The corresponding Stokes shift is equal to about 7470 cm^{-1}. The E_g band of the octahedral site could not be detected with the used equipment as it is expected at higher energy than the accessible range. This UV spectral distribution is similar to the ST sample one. The decay curve of the UV signal was fitted with a bi-exponential curve (Figure SI3). Values of τ_1=7 ns and τ_2 = 24 ns were obtained for excitation and emission wavelength equal to 250 nm and 325 nm respectively. These two values are consistent with an allowed 5d-4f transition of trivalent cerium) but they show that for these specific wavelengths another mechanism of de-excitation has to be taken into account.

In addition to the UV band, the CP sample presents a contribution centered at 525 nm. The presence of $CaSnO_3$ traces has been discarded as the emission and excitation wavelengths of the bleu-green band do not coincide with the signal reported in ref [18] (see also Figure SI4, excitation and emission curves). However we considered the potential introduction of hydroxyl groups at the F^- site. As the size of OH^- group is close to that of F^-, no significant shift was detected by X-Ray diffraction. Nonetheless, we can argue that the remaining hydroxyl groups at F^- sites in the CP sample must not be neglected. ^1H MAS-NMR experiments were then performed on both CP and ST samples, ST sample being considered without any hydroxyl group at F^- sites in the material bulk. The NMR spectra (Figure 6) exhibit several overlapping ^1H signals that may be associated with protons involved in weak hydrogen bonds (isotropic chemical shift: +1.25 ppm), chemi- or physi-sorbed water (isotropic chemical shifts ranging from +3 to +5 ppm) or hydroxyl groups substituting for F^- (broad signal centered at +6-7 ppm) [20]. Nevertheless, the width of the observed signals (mainly due to strong homo- and/or hetero-dipolar interactions) makes these discriminations hazardous, especially for the CP sample. Whatever the synthetic route, the ^1H MAS-NMR signal is detected and the CP sample does not show a significant concentration of OH^- groups in substitution of the structural F^- anions in comparison with the ST sample. This excludes a direct relationship between the presence of hydroxyl groups and the visible contribution.

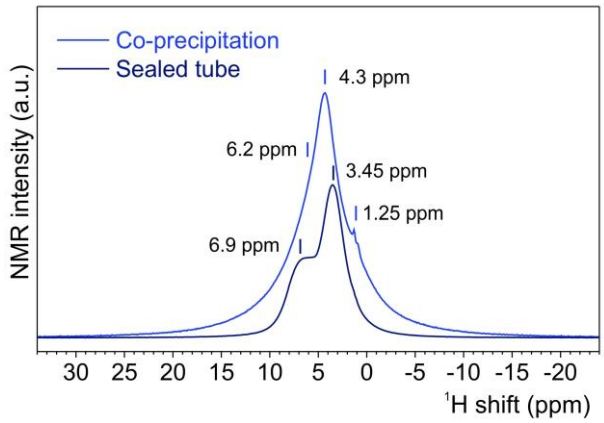

Figure 6: ^1H MAS (spinning rate: 30 kHz) NMR spectra of Ce-doped $CaSnF_6$ samples prepared by co-precipitation route (CP sample) and sealed tube synthesis (ST sample).

The stability of Ce^{3+} within the host lattice may be compensated by fluorine vacancies or reduction of Sn^{4+} at the divalent oxidation state. Indeed, a potential fingerprint of Sn^{2+} has also to be considered since both Ce^{4+} and Sn^{4+} are not expected to be optically active ions. The luminescence of Sn^{2+} was reported

in different matrices as phosphate, borax and germanate glasses under excitation at 250 nm[21]. It consists of large emissions bands ranging from 380 nm to about 650 nm. Emissions of isolated Sn^{2+} and dimers were detected later in CaSe at around 522 nm and 581 nm, respectively[22]. One can also cited the emission observed in Sn-doped K_2ZnI_4, CaSe [23] or the luminescence of Sn^{2+} in alkali binary halide phosphors such as KCl [24-26], KBr [27-30], KI [31-35], NaCl [36]. But the lack of Sn^{2+} ions in the CP- and ST samples has been checked by Mössbauer spectroscopy (Figure SI5). The charge compensation induced by the introduction of Ce^{3+} in the matrix can be obtained by the departure of fluorine anions creating a $V_F^{\bullet}$ vacancies or an intertiticial F^- anion associated to a Ce^{3+} ion substitution at one Ca^{2+} cation site. This last hypothesis has been rejected since the strontium is deficient taking into account the targeted Ca/Sr ratio (see chemical analysis) and since attempts to substitute Ca^{2+} with Ce^{3+} have all led to the formation of SnO_2 phases. Recently, luminescence of a Ce-doped double perovskite of formula Cs_2SnCl_6 has been published [37]. Considering previous studies based on Bi^{3+}-doped Cs_2SnCl_6, the authors totally discard the fact that the observed emission could be ascribed to the 5d-4f radiative transition of Ce^{3+} [38]. They conclude that the introduction of the rare earth element increases the stabilization of local point defects such as $[Ce^{3+} + V_{Cl}]$ and/or $[Sn^{2+}{}_{Sn4+} + V_{Cl}]$ from which a radiative contribution is observed. The corresponding emission is visible at 455 nm under a 350 nm excitation wavelength. However, since no visible band is detected in the Ce-doped $CaSnF_6$ ST sample, a significant concentration of localized point defect $[Ce^{3+} + V_F^{\bullet}]$ in the CP sample could explain the second contribution. Indeed the drastic variation of the surface nature and the crystallinity difference between the CP and the ST compounds (see XRD Figure 1.) should impact the spatial distribution of both Ce^{3+} and $V_F^{\bullet}$ defects. A significant difference in the local environment of fluorine between CP and ST samples was revealed by ^{19}F MAS NMR (Figure 7). The isotropic chemical shifts of the observed resonance lines are in the range of ^{19}F NMR signals reported for various elpasolite-type fluorides [39,40]. The NMR spectrum of ST exhibits a main signal at -163 ppm associated with regular MF_6 octahedra and a weak resonance line at -109 ppm which could be due to fluorine anions with a perturbed environment, for instance with a paramagnetic Ce^{3+} - $V_F^{\bullet}$ defect in its vicinity. Indeed, the nature and distribution of the surrounding cations and defects can strongly influence the ^{19}F chemical shift as well as slight deviation from the cubic symmetry. This is clearly illustrated by the multiple resonance lines observed for the CP sample (Figure 7 and Figure SI6).

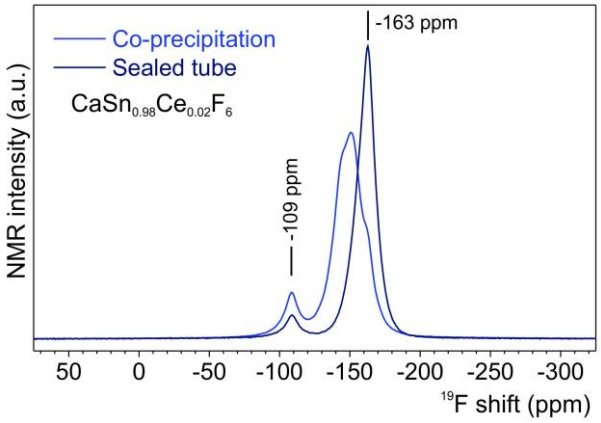

Figure 7: ^{19}F MAS (spinning rate: 30 kHz) NMR spectra of Ce-doped $CaSnF_6$ samples prepared by co-precipitation route (CP sample) and sealed tube synthesis (ST sample).

For the ST compound, the high annealing treatment that induces the crystallite growth should favor the migration of two structural defects towards the crystal surfaces and the potential resulting emission may thus be quenched (de-activated). To reinforce our interpretation, the CP compound was submitted to a second HF reductive treatment. This results in the decrease of the 525 nm emission band and confirms the thermal history effect on the emission signal (Figure SI7). By consequence, the HF heat-treatment of the raw powder after the co-precipitation appears to be crucial. We should reasonably consider that the previously presented visible emission, is not due to the presence of stabilized Sn^{2+}; it is neither related to remaining hydroxyl groups but more surely due to a coupling between the Ce^{3+} ions and local point defects such as F^- vacancies/surface defects, *i.e.* in agreement with the proposition of Zhang *et al.* on Ce-doped Cs_2SnCl_6 double perovskite.[37]. This defect contribution is strongly linked to the crystallinity of the compound as it is strongly modified by the heat-treatment.

3.4 Photochromic properties of Ce-doped $CaSnF_6$ samples.

In order to check if the CP and ST stannate fluorides possess equivalent photochromic properties as the ones reported in the Ce-doped Rb_2KInF_6 compound, the stability of the two emission bands under prolongated irradiation (20 hours) has been checked. The results obtained on both the CP and ST sample are illustrated in Figure 8.

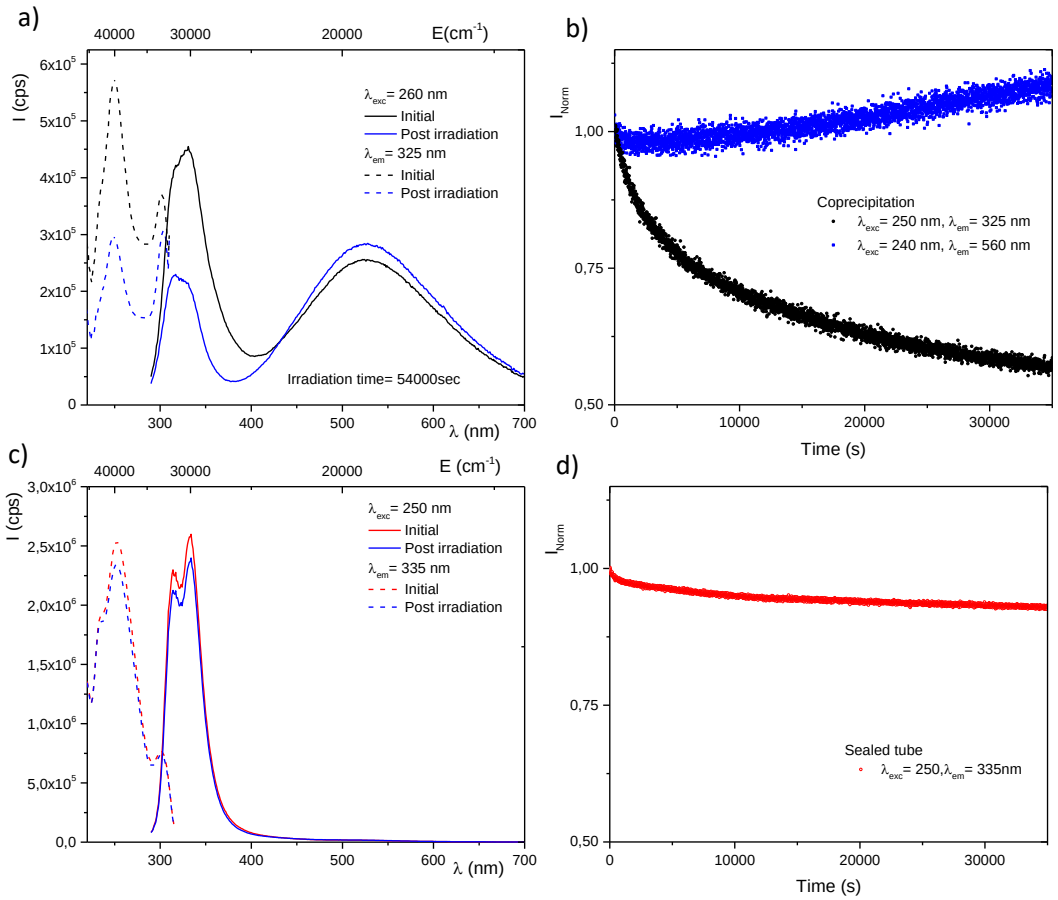

Figure 8: Excitation and emission spectra of Ce-doped $CaSnF_6$ samples: for the co-precipitation (CP) route sample irradiation time (54000s) (a); for the sealed tube synthesis (ST) sample (irradiation time 43200s) (c) and, evolution versus irradiation time of the emission band located at 325 and 560 nm for the two samples, respectively (b and d).

For both the samples, we observed a decrease of the Ce^{3+} UV (325-335 nm) emission intensity, but with a significant amplitude only for the CP sample. The figure 8b shows that the cerium intensity is divided by a factor equal to about 2 for the CP sample after 10 hours whereas the figure 8d shows that only 8% intensity is lost concerning the ST sample after 10 hours of irradiation. A satisfying fit of the evolution curve of the intensity of the CP UV emission band has been obtained using the following equation (Figure SI8a):

Equation 3: $(100\text{-}A\text{-}B)\exp(-k_1t)+B\exp(-k_2t)+A$ with, for illustration for the CP sample, A= 50.213; B= 15.706; $k_1= 7.05\text{x}10^{-05}\ s^{-1}$; $k_2= 69.22\text{x}10^{-05}\ s^{-1}$.

This model gives satisfying results for the CP sample but it is not sufficient to fit the ST kinetic curve for which the experimental acquisition was not long enough (Figure SI8b). The need to introduce two

contributions in the kinetic curve of the Ce^{3+} emission intensity for the CP sample reflects the fact that several mechanisms are involved in the cerium temporal instability under UV irradiation as for example a surface and a bulk effect.

In a concomitant time, a light intensity increase of the defect related emission band (in the visible range) is clearly detected for the CP sample (increase of the signal equal to about 10%); the dynamic observed is probably due to a spatial reorganization of the (Ce^{3+} and $V_F^{\bullet}$) species inside the crystallographic network and the surface activity under irradiation. However, no change of the spectral distribution is observed whatever the sample. The irradiation reinforces the contribution of the pre-existing defects and discards definitively a potential redox process between Sn^{4+} and Ce^{3+} ions as the origin of the photochromism (the appearance of a new Sn^{2+} contribution is not detected under irradiation). As a consequence, we suggest that the decrease of the UV Ce^{3+} emission coinciding with the slight increase of the visible band should originate from two mechanisms. On one hand, the irradiation makes possible the coupling of Ce^{3+} center and $V_F^{\bullet}$ defect due to their respective migration through the matrix. On the other hand, the excitation allows the transfer and trap of the single electron on a fluorine vacancy located at the vicinity of a Ce^{3+} ion (*i.e.* a vacancy, which is initially devoid of any electron). The second hypothesis seems to be more probable. It should be written as follows:

Equation 4- $Ce^{3+} + V_F \rightarrow Ce^{4+} + V_F^{-}$

or in the following equation, according to the Kröger-Vink's notation $Ce'_{Sn} + V_F^{\circ} \rightarrow Ce_{Ce}^{X} + V_F^{X}$ (for a more detailed explanation of this notation, see the section 4) entitled "Theoretical approach").

The kinetic behavior of the CP sample heat-treated two times under HF is slightly different. The loss of Ce^{3+} contribution remains significant but the visible band which contribution is reduced after the second heat-treatment appears quite stable (Figure SI9). This tends to validate the heat-treatment effect on the segregation of pairs of defects from the bulk to the surface of the grains and to establish a direct link between this defect and the origin of the visible band. The cerium temporal stability of the sample has been checked after storage in a dark environment at room temperature on this CP HF re-heat-treated sample. After a 350 h of relaxation, the Ce^{3+} ions intensity is recovered at about 13% of its initial level (Figure SI4 pink curve), which indicates a slow reversibility of the photo-induced process. One can say that the energetic barrier between the trapped electron level and that of the Ce^{3+} ion is not deep enough to definitively stabilize the pairs of defects. As a result, the system relaxes slowly with time.

In complement, ^{119}Sn Mössbauer spectra of CP sample is proposed before and after irradiation in Figure SI10. Results confirms the lack of Sn^{2+} stabilization but a light increase of the isomeric displacement of the Sn^{4+} (F_6) is observed (shift from -0.55mm/s to -0.45 mm/s), which may reflects a modification of the nucleus electron density.

The ^{19}F NMR signal of the CP sample after irradiation is illustrated on Figure 9.

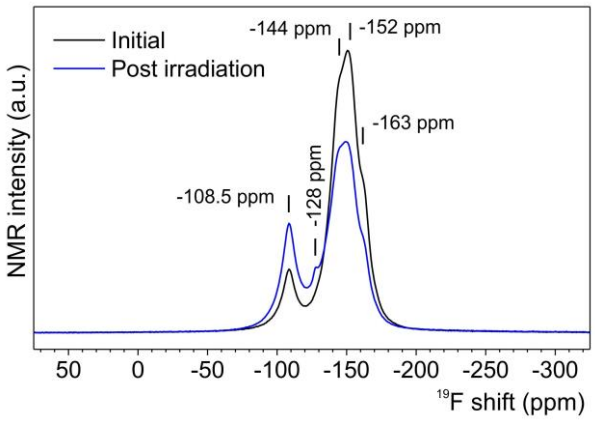

Figure 9: ^{19}F MAS-NMR spectra of the CP sample before and after irradiation.

After irradiation a significant drop of the -150-ppm signal is observed in parallel with an increase of a signal at -128 ppm showing the influence of the paramagnetic species induced by the irradiation process. The -109-ppm signal is nearly multiplied by two which seems to confirm a modification of the paramagnetic centers around the fluorine ions while the compound is irradiated. This observation is therefore in good agreement with our consideration of an emissive spectrum modification under irradiation due to an electronic transfer from the Ce^{3+} ions though the fluorine anionic vacancies.

4- Theory approach

In view of initiating a series of computational modelling approaches on these compounds with the purpose of reaching structure-property relationships and to provide a first step towards the characterization of point defects in this Ce^{3+} doped $CaSnF_6$ matrix, a theoretical DFT investigation is proposed. It relies on a chemistry defect model, which is consistent with the fluorine-deficient $CaSn_{0.98}Ce_{0.02}F_{6-\delta}$ compound, as concluded from experimental measures. Indeed, elucidating the defect chemistries in these

materials appears as crucial regarding the role played by the point defects on the photochromic properties. In the current work, the objective is to evaluate the most suitable location of the doping element by considering it solely as a trivalent species, according to the defect chemistry suggested from the experiment. A low defect concentration is investigated (1 tin ion (out of 32) is substituted with 1 cerium ion and 1 fluorine ion (out of 192) is removed, *i.e.* $CaSn_{0.96875}Ce_{0.03125}F_{5.96875}$), which is consistent with experimental conditions. By taking into account a 2x2x2 supercell approach (made of 255 ions), this hypothesis consists in considering the following balanced charge and mass reaction (according to Kröger–Vink's notation) in which we suppose that Cerium is exclusively at the +III oxidation state:

Equation 5- $null \xrightarrow{CeF_3} Ce'_{Sn} + V_F^{\circ} + 2F_F^{\times} + \frac{1}{2}F_2$

This reaction is based on a nomenclature, where the charge state of an impurity or defect indicates the charge relative to the host material. Here, it involves the substitution of Cerium for Tin at its normal site in the lattice, thus resulting in the creation of a $\mathrm{Ce}'_{\mathrm{Sn}}$ point defect (the minus 1 effective charge of this point defect (indicated as exponent in the Kröger–Vink's notation) being linked to the initial +IV oxidation state characterizing the Sn^{4+} site). Indeed, to maintain the electroneutrality of the crystal, the occurrence of such defect is considered along with the appearance of a fluoride vacancy, *i.e.* $\mathrm{V}_{\mathrm{F}}^{\circ}$ (characterized by a +1 positive effective charge, also indicated as exponent), which is required to compensate -1 charge of $\mathrm{Ce}'_{\mathrm{Sn}}$.

For this mechanism of Cerium incorporation into the matrix – by supposing it solely in the +III oxidation state as stated before – several models of configuration can be listed by varying the relative distance between the two kinds of point defects, $\mathrm{Ce}'_{\mathrm{Sn}}$ and $\mathrm{V}_{\mathrm{F}}^{\circ}$. The positioning of the sole $\mathrm{V}_{\mathrm{F}}^{\circ}$ was chosen as the most possible central location within the 2x2x2 supercell (0.63263 ; 0.5 ; 0.5) while the Ce^{3+} ion was thus placed at different initial sites of $\mathrm{Sn}_{\mathrm{Sn}}^{\mathrm{x}}$ (Figure 10): i) configuration i (magenta polyhedron) corresponding to the closest position of Ce from the vacancy involving (*i.e.* (0.75; 0.5; 0.5)), for which the resulting $\mathrm{Ce}'_{\mathrm{Sn}} - \mathrm{V}_{\mathrm{F}}^{\circ}$ distance before relaxation is equal to 1.98 Å; ii) configuration t (green polyhedron) linked to the $\mathrm{Ce}'_{\mathrm{Sn}}$ defect placed at (0.5; 0.5; 0.75), with an initial $\mathrm{Ce}'_{\mathrm{Sn}} - \mathrm{V}_{\mathrm{F}}^{\circ}$ distance equal to 4.77 Å; iii) configuration m (yellow polyhedron) with $\mathrm{Ce}'_{\mathrm{Sn}}$ at (0.75; 0.25; 0.25)) for which the resulting $\mathrm{Ce}'_{\mathrm{Sn}} - \mathrm{V}_{\mathrm{F}}^{\circ}$ distance before relaxation amounts to 5.96 Å; iv) configuration j (orange polyhedron) characterized by $\mathrm{Ce}'_{\mathrm{Sn}}$ at (0.75; 0.5; 1)) with an initial distance $\mathrm{Ce}'_{\mathrm{Sn}} - \mathrm{V}_{\mathrm{F}}^{\circ}$ of 8.66 Å and finally, v) configuration p (blue polyhedron) for $\mathrm{Ce}'_{\mathrm{Sn}}$ located at (0.5; 0.25; 1), involving the largest initial $\mathrm{Ce}'_{\mathrm{Sn}} - \mathrm{V}_{\mathrm{F}}^{\circ}$ distance, which is equal to 9.69 Å. The

radius value of Sn(+IV) in an octahedral site (coordination [VI]) is 0.55 Å, while the corresponding value for the Ce(+III) ion is 1.01 Å. There is thus a great differentiation between the size of the doping ion and that of the ion belonging to the host matrix that is substituted, with almost a factor of 2 between both ionic radii. This already indicates that the cerium placed in this cationic site has to increase cation-Fluor distances through ion relaxation. Table SI1 illustrates the structural changes induced by Ce doping in the $CaSnF_6$ matrix accompanied by the concomitant creation of the fluorine vacancy while the corresponding local geometry evolution is highlighted in Figure 10. First of all, it is possible to estimate the effect that the formation of the two above-mentioned point defects has on the cell volume. The absolute volume change with respect to the one characterizing the undoped system, |ΔV/V|, is ranging from to 3.9 to 7.7 %, the configuration i corresponding to the largest value (+7.7 %), with a positive value of ΔV/V, thus being characterized by an expansion of the unit cell volume. On the other hand, all other configurations are linked to a unit cell volume decrease upon substitution (*i.e.* supercell compression), all of them involving a ΔV/V of -3.9 %.

With respect to the size mismatch between the ionic radii of dopant and host cation, the consideration of the geometry features after relaxation (Figure SI11) indeed indicates that upon substitution of an Sn^{4+} atom by a Ce^{3+} one in the octahedral site, a change in the polyhedron volume occurs but the local octahedral site symmetry is preserved for all configurations apart from the configuration i, with only very slight or almost no distortion (as already indicated through the observation that all interatomic Ce-F distances of the polyhedra are identical). Moreover, by focusing on various descriptors able to account for and to quantitatively measure the extent of the octahedral deformation (Figure S11), this conclusion can be definitely confirmed for the configurations t, m, j and p. The various distortion indices such as the quadratic elongation, λ [41], the bond angle variance, σ^2 [42-45], and the Baur's distortion index (D) [46] are almost equal to the values expected for a perfect octahedron (*i.e.* 1, 0 and 0, respectively (Figure SI11)). On the other hand, the comparison of the SnF_6 and CeF_6 polyhedron volume (V_{pol}), for the undoped and the doped compounds in the configurations t, m, j and p respectively clearly demonstrates that a consequent expansion occurs upon substitution in order to leave sufficient space around the Cerium (*i.e.* ~13.3 $Å^3$ against ~10.3 $Å^3$ for the doped and undoped systems, respectively). After full structural relaxations, it is also possible to notice that the $Ce'_{Sn} - V_F^{\circ}$ distance is modified as follows: 1.95 Å, 4.72 Å, 5.87 Å, 8.54 Å, and 9.56 Å for the configurations i, t, m, j and p, respectively (Figure 10). This corresponds to a shortening of the initial $Ce'_{Sn} - V_F^{\circ}$ distance of 0.03 Å, 0.05 Å, 0.09 Å, 0.12 Å, and 0.13 Å

for the configurations i, t, m, j and p, respectively. At variance with other configurations, configuration i induces naturally an effective coordination number ($ECoN$) [43-45] of ~5 instead of ~6 for all other configurations. It introduces obviously a larger distortion index than for other cases, in link with the distinct Ce-F distances of the polyhedron originating from the vacancy having replaced one of the six F atoms. For this CeF_5 polyhedron, interatomic distances range from 2.11 Å to 2.21 Å (thus involving an average value (l_{av}) of 2.152 Å, which is only very slightly higher than the 2.151 Å characterizing the other configurations, for the various CeF_6 octahedra). These values exhibit significant increase with respect to the Sn-F distance of 1.98 Å characterizing the regular SnF_6 octahedron in the pristine material.

From the energetics point of view, these various cases corresponding to the same chemical formula can be directly compared and thus be classified in terms of relative energies (Figure 11). The most stable configuration is clearly i (all other ones being characterized by an energy per formula unit (p.f.u.), which is larger by at minimum 479 meV). In terms of energy ranking classification, this most stable configuration is first followed by t, then by m, p and j (this latter case corresponding thus to the configuration with the highest energy p.f.u. with respect to i; *i.e.*: 504 meV). These preliminary results indicate that the formation of $\mathrm{Ce}'_{\mathrm{Sn}} - \mathrm{V}_{\mathrm{F}}^{\circ}$ pairs of defects is more stable than the location of a fluorine vacancy on other sites, farther than the location as first neighbour and thus avoiding any clustering of point defects. This observation can be related to the fact that for the configuration i, the CeF_5 polyhedron preserves sufficient space for the Ce^{3+} ion (with even slightly larger Ce-F interatomic distances than for other arrangements) while such relative positioning of the two point defects nearby from each other (with the Ce^{3+} first neighbour to the vacancy) introduces a much larger favourable electrostatic attraction than all other ones for which the cerium is farther with respect to the vacancy (thus involving a lower attractive stabilization energy). The preferential positioning of a fluorine vacancy at the vicinity of Ce^{3+} may allow this anionic vacancy to act as an electron trap. Thus, the pairing of $\mathrm{Ce}'_{\mathrm{Sn}}$ and $\mathrm{V}_{\mathrm{F}}^{\circ}$ in the crystallographic network should lead to the potential oxidation of the rare earth element at the +IV oxidation state along with an electron transfer to the adjacent anionic vacancy (*i.e.* stabilization through a colour center or an F-center, corresponding to this neutral vacancy: $\mathrm{V}_{\mathrm{F}}^{\mathrm{X}}$). Therefore, this first series of calculations, which will be followed by further theoretical works calling especially to other functionals and focusing on electronic structure, already tend to confirm the hypotheses proposed to explain the photochromism observations for the Ce^{3+}-doped $CaSnF_6$ compound through the prevalent first neighbour localization of $\mathrm{Ce}'_{\mathrm{Sn}}$ and $\mathrm{V}_{\mathrm{F}}^{\circ}$. Further calculations will also be performed by involving other defects chemistry to decipher in

particular the role of Ce^{4+} in the matrix (Ce_{Sn}^{x}) since magnetic measurement confirm a non-negligible concentration of this tetravalent ion.

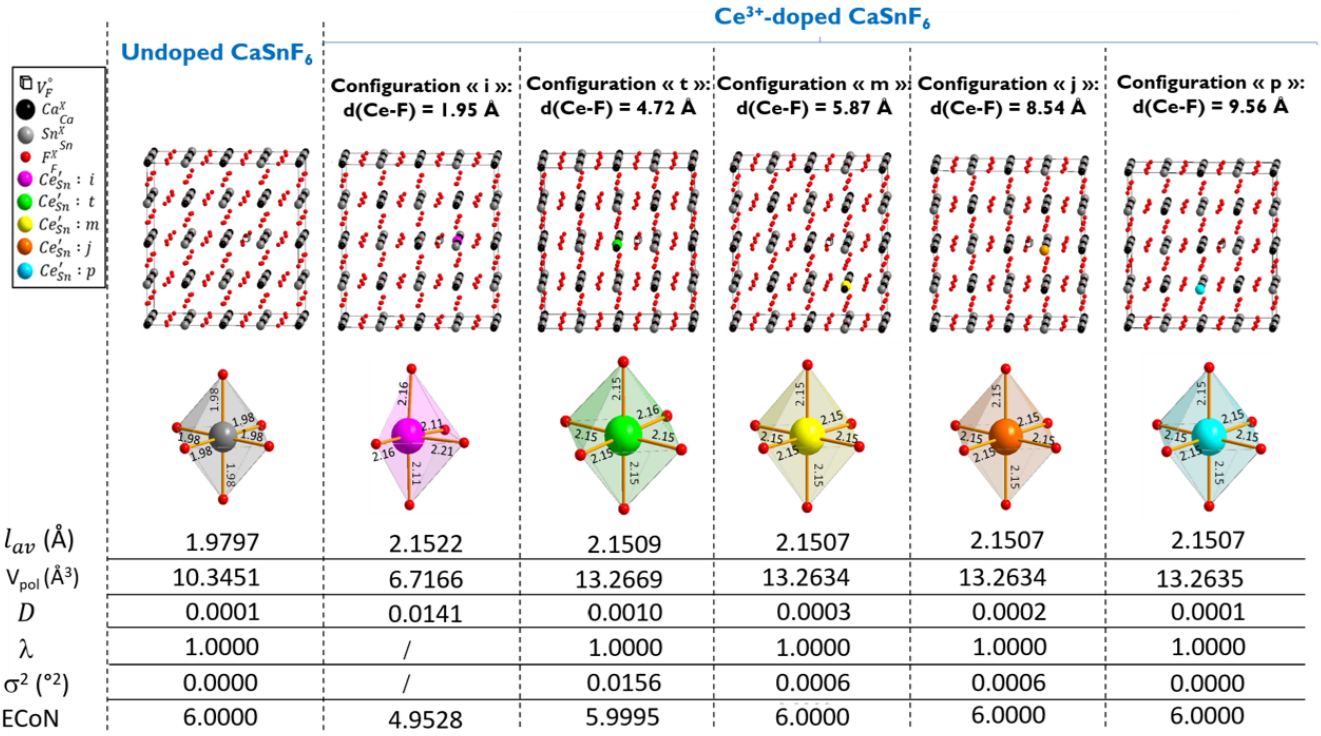

	Undoped $CaSnF_6$	Configuration « i »: d(Ce-F) = 1.95 Å	Configuration « t »: d(Ce-F) = 4.72 Å	Configuration « m »: d(Ce-F) = 5.87 Å	Configuration « j »: d(Ce-F) = 8.54 Å	Configuration « p »: d(Ce-F) = 9.56 Å
l_{av} (Å)	1.9797	2.1522	2.1509	2.1507	2.1507	2.1507
V_{pol} (Å³)	10.3451	6.7166	13.2669	13.2634	13.2634	13.2635
D	0.0001	0.0141	0.0010	0.0003	0.0002	0.0001
λ	1.0000	/	1.0000	1.0000	1.0000	1.0000
σ^2 (°²)	0.0000	/	0.0156	0.0006	0.0006	0.0000
ECoN	6.0000	4.9528	5.9995	6.0000	6.0000	6.0000

Figure 10- Top: Representations of the relaxed 2x2x2 supercells for the undoped (Left) and Ce^{3+}-doped $CaSnF_6$ (Right: i, t, m, j and p configurations, successively) matrices; the interatomic distance d_{Ce-F} after relaxation for the doped system is indicated. Middle and Bottom: Illustrations and structural features of the corresponding involved polyhedra (SnF_6 for the undoped system and CeF_6 for the substituted matrices) including the average bond length (l_{av}), the polyhedron volume, the Baur's distortion index (D), the quadratic elongation (λ), the bond angle variance (σ^2) and the effective coordination number (EcoN).

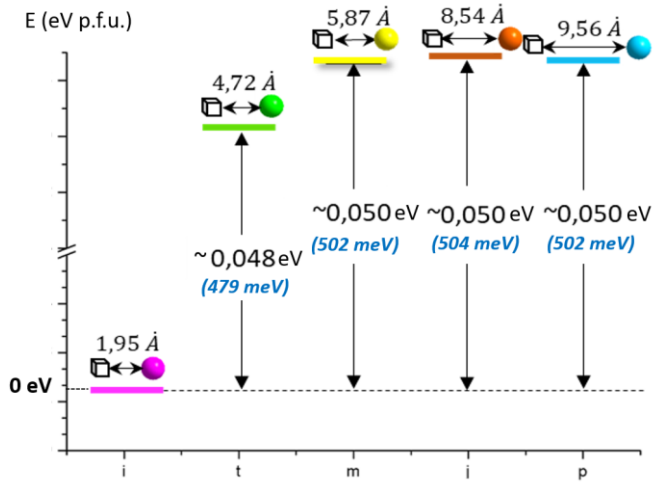

Figure 11- Energy ranking for the 2x2x2 supercells of Ce^{3+}-doped $CaSnF_6$ considered within various configurations by taking into account the joined creation of one substituted Ce'_{Sn} and one compensating fluorine vacancy V_F° (Most stable configuration, i, placed at E(p.f.u.) = 0.000 eV): i, (on the left) along with t, m, j and p configurations by considering the various relative positioning of the (Ce'_{Sn}) and (V_F°) point defects. The distance between both defects after relaxation is indicated above each energy level.

5- Conclusion

Ce^{3+} doped-$CaSn(OH)_6$, $CaSnO_3$ and have been synthesized though a coprecipitation process with a good purity and an advanced structural investigation highlights a cationic disorder on the Ca^{2+} and Sn^{4+} general position. Chemical analysis confirms the good introduction of cerium cationic at the targeted concentration with a proportion of Ce^{3+} equal to one third of the total amount in the fluorine compound (magnetism). The luminescence of Ce^{3+} in the oxygenized matrices is quenched whereas it has been clearly detected in the fluorine compound. The magnetic response suggests the existence of single electrons potentially trapped on the fluorine vacancy. An additional visible contribution strongly related to the synthesis route appears. Its assignation to Sn^{2+} center has been discarded by Mössbauer spectroscopy and the fact that it is sensible to the heat-treatment. We attribute its origin to the existence of surface and bulk defect which can be neutralized by successive heat-treatments due to migration and passivation at the surface.

The photochromic properties of the Ce^{3+} doped-$CaSnF_6$ are significant given that 50% of the maximum intensity is lost after 10h of irradiation but this phenomenon is linked to the initial defect concentration as results observed on the compound prepared through the sealed tube method are much weaker. A natural bleaching of the photochromism was observed which confirms the metastable character of the system after irradiation. Complementary characterization performed by Sn(IV) Mössbauer spectroscopy and F^{19} RMN revealed the activation of defects contribution under light –matter interaction and an additional local disorder around Sn^{4+} cations and F^- anions. This is compatible with the mobility effects and the possible electron trap on the vacancies. Although further investigations may be required to ascertain a full microscopic model for photochromic centers about their nature and dynamics, the computational approach already provides some interesting insight. Indeed, the DFT investigations reveal that upon substitution of a Sn^{4+} ion by a Ce^{3+} one in the initially octahedral site accompanied with the creation of fluorine vacancy, the lowest energy among various configurations involving several distances between both kinds of defects is reached for the vacancy directly belonging to the Ce-containing polyhedron. This

favourable location of the Ce^{3+} close to the fluorine vacancy can be exploited to propose a plausible mechanism accounting for the photochromic properties of Ce-doped $CaSnF_6$. This phenomenon could thus be linked to the local reorganization of electrons within $\{Ce'_{Sn} - V_F^{\circ}\}^x$ defects clusters, therefore involving a potential electronic transfer from the Cerium 5d orbitals to the adjacent vacancy thus becoming neutral in the form of V_F^X (*i.e.* stabilization through a colour center or an F-center). By considering such defect chemistry as prevalent according to ICP measurements, the rising number of created pairs of defects (i.e. complexes involving a trapped electron associated with a Ce^{4+} ion) will thus influence the efficiency of the electronic transfer and in turn enhance the extent of the photochromism considered as occurring under the impulsion of the creation of this kind of defects.

Acknowledgements

This investigation was supported by the CNRS and the Nouvelle Aquitaine region. This study was carried out with financial support from the French State, managed by the French National Research Agency (ANR) in the frame of a non-thematic programs (PRIDE - ANR-16-CE08-0029) and in the frame of "the Investments for the future" Program IdEx Bordeaux – LAPHIA (ANR-10-IDEX-03-02). This work was granted access to the HPC resources of IDRIS under the allocation 2019-[A0070806732] made by GENCI and was also performed using the facilities and computing time of the supercomputer center MCIA of the University of Bordeaux and Pays de l'Adour and the HPC resources from DSI-CCUB (University of Burgundy).

REFERENCES

[1] G. P. Smith, *J. Mater. Sci.*, 2(2) (1967) p. 139

[2] R. Zhang, « The Syntheses, NMR and Photochromic Properties of Modified Dimehtyldihydropyrenes », B.Sc. University of Science and Technology of China ISBN: 978-0-494-41217-6 (1993)

[3] T. He, Y Ma, Y Cao and P. Jiang, *Langmuir*, 17(26) (2001) p. 8024, doi: 10.1021/la010671q

[4] Y. Guo, D. Zhang, J. Wang, H. Lu, and S. Pu, *Dyes Pigments*, 175 (2020) p. 108191, doi: 10.1016/j.dyepig.2020.108191.

[5] A. A. Ali, R. Kharbash and Y. Kim, *Anal. Chim. Acta*, 1110 (2020) p. 199, doi: 10.1016/j.aca.2020.01.057.

[6] L. A. Harrah, « Photochromic radiation dosimeter », US3609093A, (1968).

[7] M. Irie, S. Irie, S. Maeda and Y. Tanaka, « Photochromic composition and dosimeter », JP2002285146A.

[8] O. J. X. Morel and R. M. Christie, *Chem. Rev.*, 111(4) (2011) p. 2537, doi: 10.1021/cr1000145.

[9] T. Yu. Sizova, V. Yu. Veslopolova, R. Yu. Shendrik, A. V. Egranov, E. A. Radzhapov and A. A. Shalaev, *Bull. Russ. Acad. Sci. Phys.*, 81(9) (2017) p. 1090, doi: 10.3103/S1062873817090234.

[10] J. P. Chaminade, A. Garcia, T. Gaewdang, M. Pouchard, J. Grannec and B. Jacquier, *Radiat. Eff. Defects Solids*, 135(1-4) (1995) p. 137, doi: 10.1080/10420159508229823.

[11] L. Cornu ¸M. Gaudon, P. Veber, A ; Villesuzanne, S. Pechev, A. Garcia and V. Jubera, *Chem. - Eur. J.*, 21(13) (2015) p. 5242, doi: 10.1002/chem.201405784.

[12] H. Bode and E. Voss, *Z. Fur Anorg. Allg. Chem.*, 290(1-2) (1957) p. 1, doi: 10.1002/zaac.19572900102.

[13] M. Gaudon, G. Salek, M. Kande, I. Andron, C. Frayret,E. Durand, N. Penin, M. Duttine, A. Wattiaux and V. Jubera, , *J. Solid State Chem.*, 265 (2018) p. 291, doi: 10.1016/j.jssc.2018.06.017.

[14] G. Kresse and Furthmüller, *Phys. Rev. B: Condens. Matter*, 54 (1996) p. 11169, DOI:https://doi.org/10.1103/PhysRevB.54.11169

[15] G. Kresse and D. Joubert, *Phys. Rev. B* 59 (1999) p. 1758, DOI:https://doi.org/10.1103/PhysRevB.59.1758

[16] J. P. Perdew, A. Ruzsinszky, G.I. Csonka, O.A. Vydrov, G. E. Scuseria, L.A. Constantin, X. Zhou and K. Burke, *Phys. Rev. Lett.*, 100(13) (2008) p. 136406, https://doi.org/10.1103/PhysRevLett.100.136406

[17] G. Blasse, W. Schipper and J.J. Hamelink, *Inorganica Chimica Acta*, 189 (1991) p.77, https://doi.org/10.1016/S0020-1693(00)80392-8

[18] A. Borisevitch, A. Dosovitski, A.A. Fedorov, M. Korzhik and O. Missevitch, *IEEE Transactions on Nuclear Science* 56(4, Pt. 3) (2009) 2271, DOI: 10.1109/TNS.2009.2024416

[19] Yüksel Karabulut 1 , Mehmet Ayvacikli, Adil Canimoglu, Javier Garcia Guinea, Nurdogan Can,

Luminescence, 30(4) (2015) 457, doi: 10.1002/bio.2760. Epub 2014 Sep 4.

[20] J.P. Yesinowski, E. Eckert, G.R. Rossman, *J. Am. Chem. Soc.*, 110(5) (1988), p. 1367, https://doi.org/10.1021/ja00213a007

[21] R. Reisfeld, L. Boehm and B. Barnett, *J of Solid State Chem.*, 15 (1975) 140, https://doi.org/10.1016/0022-4596(75)90237-6

[22] S. Asano, N. Yamashita and Y. Nakao, *Phys.Stat. Sol. B*, 89 (1978) 663, https://doi.org/10.1002/pssb.2220890242

[23] M.S. Pidzyrailo, V. V. Vistovsky and O.T. Antonyak, *Opt. Comm.,* 199 (2001) 149, https://doi.org/10.1016/S0030-4018(01)01592-9

[24] J. Nara and S. Adachi, *J. Appl. Phys.*, 110(11) -2011) p. 113508, doi: 10.1063/1.3664916.

[25] V. Hizhnyakov, S. Zazubovich, and T. Soovik, *Phys. Status Solidi B*, 66(2) (1974) p. 727, doi: 10.1002/pssb.2220660238.

[26] Zh. Egemberdiev, V. Seeman, S. Zazubovich, and N. Jaanson, , *Phys. Status Solidi B*, 92(1) (1979) p. 335, doi: 10.1002/pssb.2220920139.

[27] A. Fukuda, *Phys. Rev. B*, 1(10) (1970) p. 4161, doi: 10.1103/PhysRevB.1.4161.

[28] R. Aceves, U. Caldiño G, J. Rubio O, and E. Camarillo, *J. Lumin.*, 65(3) (1995) p. 113, doi: 10.1016/0022-2313(95)00069-3.

[29] T. Tsuboi and P. Silfsten, *Phys. Rev. B*, 43(2) (1991) p. 1777, doi: 10.1103/PhysRevB.43.1777.

[30] A. Scacco and P. W. M. Jacobs, *J. Lumin.*, 26(4) (1982), p. 393, https://doi.org/10.1016/0022-2313(82)90067-9

[31] D. Simkin, J. P. Martin, L. S. Dang and Y. Kamishina, *Chem. Phys. Lett.*, 65(3) (1979) p. 569, doi: 10.1016/0009-2614(79)80293-6.

[32] L. S. Dang, P. W. M. Jacobs, and D. J. Simkin, *J. Phys. C Solid State Phys.*, 18 (18) (1985) p. 3567, doi: 10.1088/0022-3719/18/18/021.

[33] P. W. M. Jacobs, Y. Kamishina, L. L. Coatsworth, and M. J. Stillman, *J. Lumin.*, 18-19 (1979) p. 619, doi: 10.1016/0022-2313(79)90205-9.

[34] J. De Kinder, E. Goovaerts, and D. Schoemaker, *Solid State Commun.*, 66(11) (1988) p. 1145, doi: 10.1016/0038-1098(88)91121-0.

[35] Y. Kamishina, V. S. Sivasankar, and P. W. M. Jacobs, *J. Chem. Phys.*, 76(10) (1982) p. 4677, doi: 10.1063/1.442782.

[36] M. Kondo and S. Adachi, *ECS Journal of Solid state Science and technology*, 2(1) (2013) R9, https://doi.org/10.1149/2.029301jss

[37] H. Zhang, L. Zhu, J. Chen, L. Chen, C. Liu and S. Yuan, *Materials* 12(9) (2019) 1501, DOI: 10.3390/ma12091501

[38] Z. Tan, J. Li, C. Zhang, Z. Li, Q. Hu, Z. Xiao, T. Kamiya, H. Hosono, G. Niu, E. Lifshitz, Y. Cheng and J. Tang, *Adv. Funct. Mater*. 28 (2018) 1801131, https://doi.org/10.1002/adfm.201801131

[39] M. Ahrens, G. Scholz, E. Kemnitz, *J of Fluorine Chemistry* 130 (2009), p. 383, 10.1016/j.jfluchem.2009.01.001

[40] H. Faget-Guengard, J.M. Bobe, J. Sénégas, A. Tressaud, J. Grannec , *J Alloy Compd*. 238 (1996), p. 49

[41] K. Robinson, G. V. Gibbs, and P. H. Ribbe, *Science (Washington, DC, U. S.)*, 172 (1971) p.567, DOI: 10.1126/science.172.3983.567

[42] R. Hoppe, *Z. Kristallogr.*, 150 (1979) p.23, DOI: 10.1524/zkri.1979.150.1-4.23

[43] R. Hoppe, S. Voigt, H. Glaum, J. Kissel, H. P. Müller, and K. Bernet, *J. Less-Common Met.*, 156(1-2) (1989) p.105, https://doi.org/10.1016/0022-5088(89)90411-6

[44] C. Ferraris, "Fundamentals of Crystallography," 2nd ed., ed. by C. Giacovazzo, Oxford University Press, Oxford (2002), p. 526

[45] W. H. Baur, *Acta Crystallogr., Sect. B: Struct. Sci.*, 30 (1974) p.1195, https://doi.org/10.1107/S0567740874004560

AUTHOR INFORMATION

Corresponding Author

Email: veronique.jubera@u-bordeaux.fr

Author Contributions

The manuscript was written through contributions of all authors. All authors have given approval to the final version of the manuscript.

Notes

The authors declare no competing financial interests.

Figure SI1-Rietveld refinements of $CaSnF_6$ compound

Refinement hypotheses

Type ①

Phase	Space group	Wickoff positions	Atomic positions	Biso	Occupation
$CaSnF_6$	F3-m3	Ca 4a Sn 4b F 24e	0 0 0 0.5 0.5 0.5 x 0 0	Free	0.02083 0.02083 0.12500
CaF_2				Free	Free

Type ②

Phase	Space group	Wickoff positions	Atomic positions	Biso	Occupation
$CaSnF_6$	F3-m3	Ca 4a Sn 4b F 24e	x y z x y z x 0 0	Free	Free Free Free
CaF_2				Free	Free

Type ③ **:** affinement rietvelt en Fm-3m du $CaSnF_6$ et de CaF_2 avec B_{iso} et taux d'occupation ouvert et inversion position de wickoff Ca et Sn/ NB : 0.01997+0.00096 =0.02093 au lieu de 0.02083

Phase	Space group	Wickoff positions	Atomic positions	Biso	Occupation
$CaSnF_6$	F3-m3	Ca 4a Sn 4a Sn 4b Sn4b F 24e	x y z x y z x y z x y z x 0 0	Free	Free Free Free
CaF_2				Free	Free

Results

Refinement type	**a(Å)**	x_F	B_{iso}**(Å)**	**Occupation**
①	8.33837(35)	0.26184(30)	Ca: 0.310(68) Sn: 0.626(32) F: 2.344(74)	0.02083 0.02083 0.12500
②	8.33862(34)	0.26445(35)	Ca: 1.084(94) Sn: 0.403(35) F: 2.946(122)	0.02235(47) 0.02075(43) 0.13340(282)
③	8.33861(34)	0.26457(34)	Ca (4a) : 1.222(101) Sn(4a) : 1.222(101) Ca(4b) : 0.330(34) Sn(4b) : 0.330(34) F : 3.040(122)	0.01997(0) 0.00096(0) 0.00096(0) 0.01997(0) 0.13518(1)
	Rp	**Chi²**	**Bragg R factor $CaSnF_6$**	**Bragg R factor CaF_2**
①	11.9	5.25	4.32	1.38
②	11.3	4.84	4.43	1.27
③	11.4	4.86	4.46	1.16

Valence bond calculation [1]

	$CaSnF_6$ type ①	$CaSnF_6$ type ②	$CaSnF_6$ type ③
d(Ca-F) (A)	2.183	2.206	2.206
Vcalc	2.39	2.25	2.24
Vthéo	2	2	2
d(Sn-F) (A)	1.986	1.964	1.962
Vcalc	4.1	4.3	4.3
Vthéo	4	4	4

$\boldsymbol{V_{cal} = \sum_j^i \exp(\frac{r_0' - r_{ij}}{B})}$ = valence calculée

Graphical results

type ①

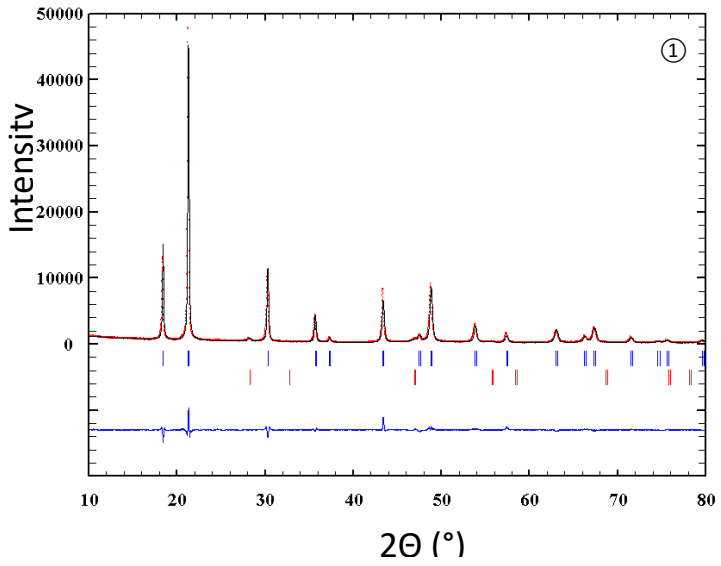

[1] I. D. Brown et D. Altermatt, « Bond-valence parameters obtained from a systematic analysis of the Inorganic Crystal Structure Database », *Acta Crystallogr. B*, vol. 41, nº 4, p. 244-247, août 1985, doi: 10.1107/S0108768185002063.

type ②

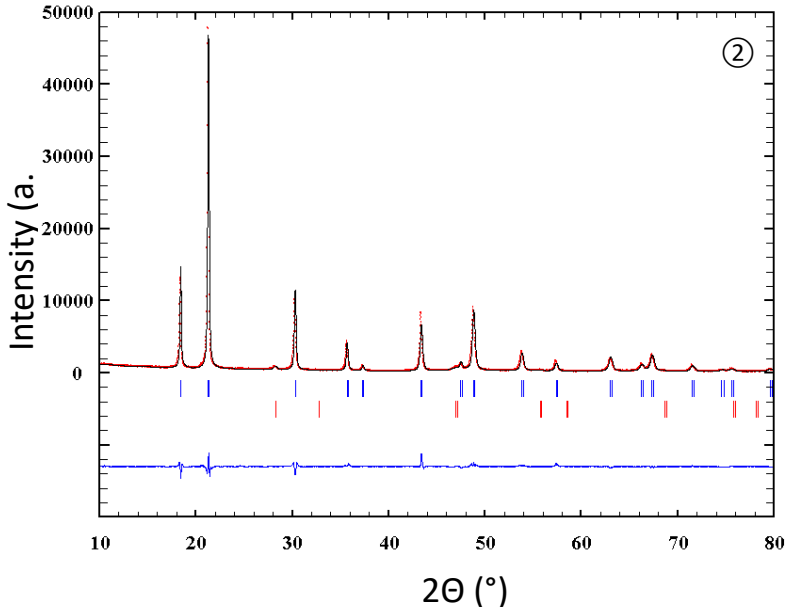

type ③

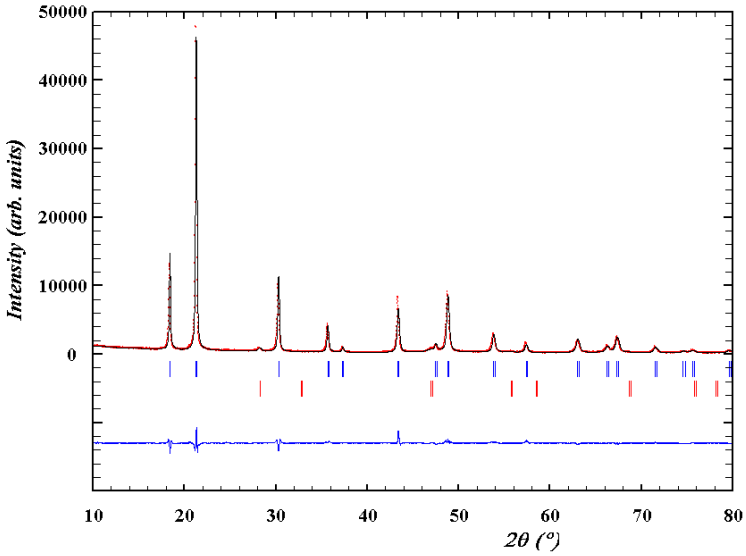

Figure SI2- Magnetism measurements performed on $CaSnO_3$ and $CaSnF_6$

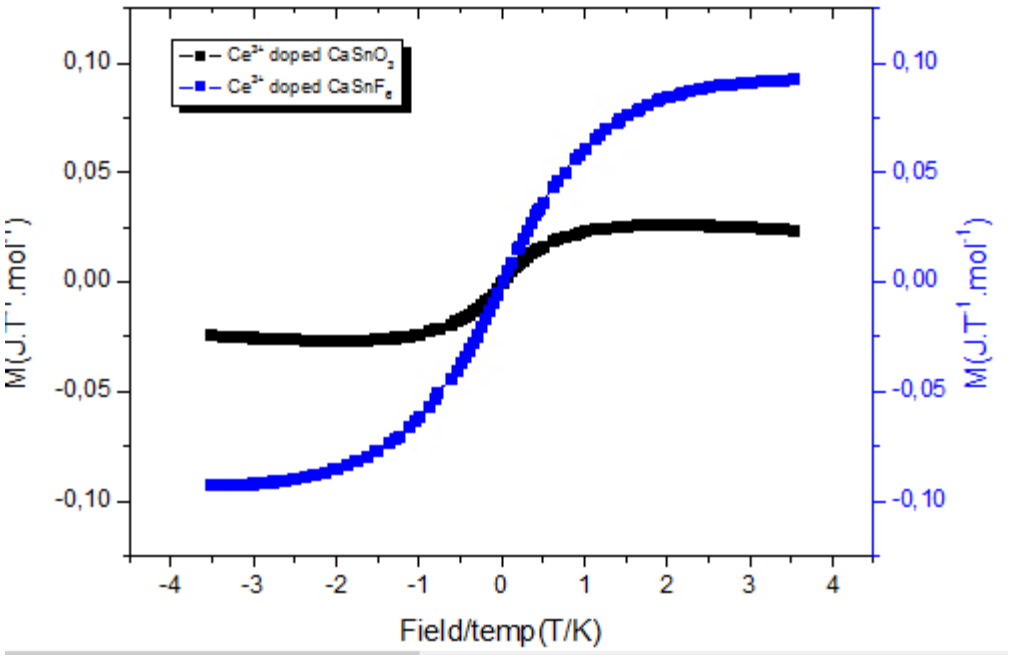

A weak paramagnetic contribution is detected on the oxide compound. One can notice a significant diamagnetic signal in coherence with a higher Ce^{4+} concentration.

Figure SI3- Decay time curve of Ce doped $CaSnF_6$

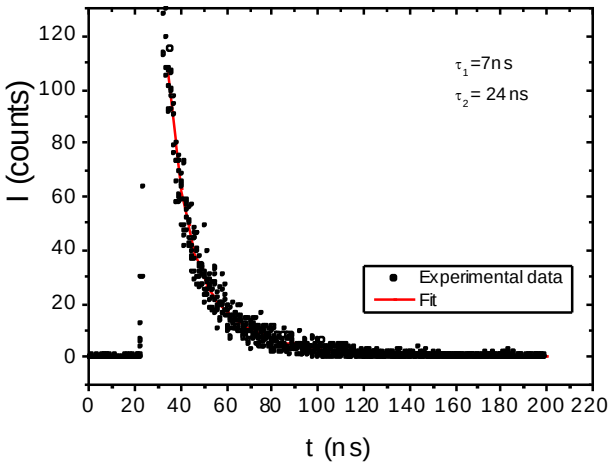

Two decay times have been extracted from this curve but one has to notice that the global signal is weak due to the power of the pulse D2 lamp.

Figure SI4- Luminescence curves of the HF heat treated CP sample at initial time (black curve), after irradiation (blue curve), after350 hours of relaxation after irradiation (red curve)

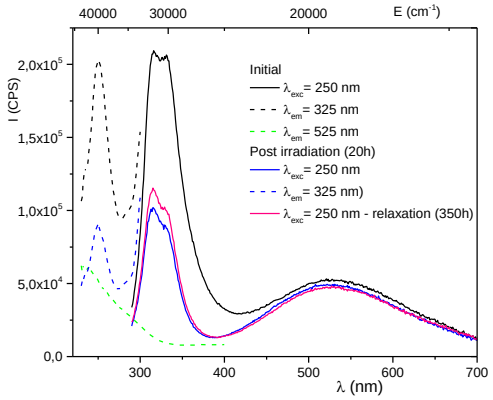

Figure SI5- Room temperature ^{119}Sn Mössbauer spectra of Ce-doped $CaSnF_6$ samples obtained by co-precipitation route and sealed tube synthesis.

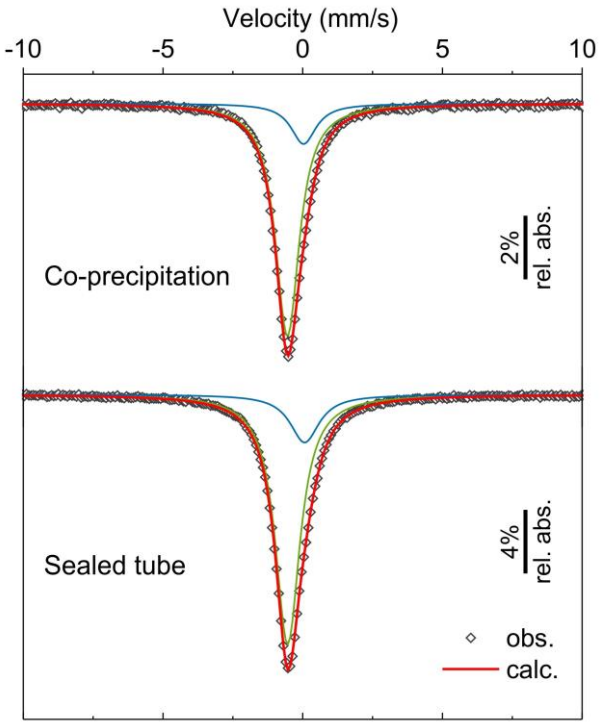

The ^{119}Sn Mössbauer spectra of both CP and ST samples are mainly composed by a singlet with a negative isomer shift δ = -0.55(1) mm/s (linewidth Γ = 1.05(2) mm/s) characteristic of Sn^{4+} in fluoride compounds [2,3,4]. Keeping in mind the limit of detection of the technique (about 0.5 mol.%) and the difference of Lamb-Mössbauer factor (f) between Sn^{4+} and Sn^{2+}, no signal due to divalent tin was detected at room temperature. A quadrupole doublet with an isomer shift around 3 mm/s and a quadrupole splitting

[2] M. Gaudon, G. Salek, M. Kande, I. Andron, C. Frayret,E. Durand, N. Penin, M. Duttine, A. Wattiaux and V. Jubera, , *J. Solid State Chem.*, 265 (2018) p. 291, doi: 10.1016/j.jssc.2018.06.017.
[3] Y. Calage, R. Tortevois, F. Varret, *J. Phys. Chem. Solids*, 51(8) (1990), p. 911, https://doi.org/10.1016/0022-3697(90)90031-A
[4] L. Fournès, P. Lagassié, Y. Potin, J. Grannec, P. Hagenmuller, *Mater. Res. Bull.*, 21 (1986), p 999, https://doi.org/10.1016/0025-5408(86)90138-8

parameter of about 1.5 mm/s is indeed expected for Sn^{2+} like for example, in $BaSn_2F_6$ or $BaSnF_4$ [5]. The other component (δ = 0.05(5) mm/s, Γ = 1.10(5) mm/s) may be associated with amorphous SnO_2 as minor secondary phase and/or under-coordinated Sn^{4+} ions in the structure of fluorine-deficient $CaSn_{0.98}Ce_{0.02}F_{6-\delta}$.

Figure SI6- ^{19}F MAS (spinning rate: 30 kHz) NMR spectra of Ce-doped $CaSnF_6$ samples prepared by co-precipitation route and sealed tube synthesis.

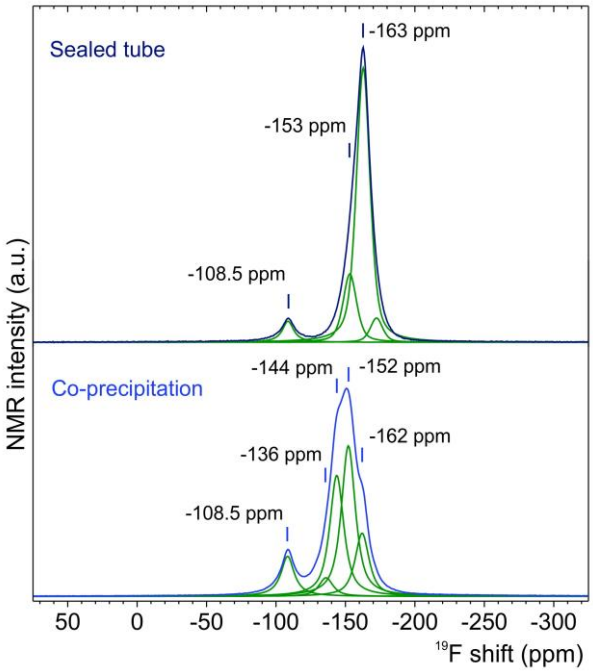

[5] G. Dénès, A. Muntasar, 153 (2004), p. 91, https://doi.org/10.1023/B:HYPE.0000024716.20800.7a

Figure SI7- Luminescence of Ce-doped CaSnF- compound ; sealed tube (red curves ; coprecipitation route after synthesis : black curves ; after heat treatment : bleu curves

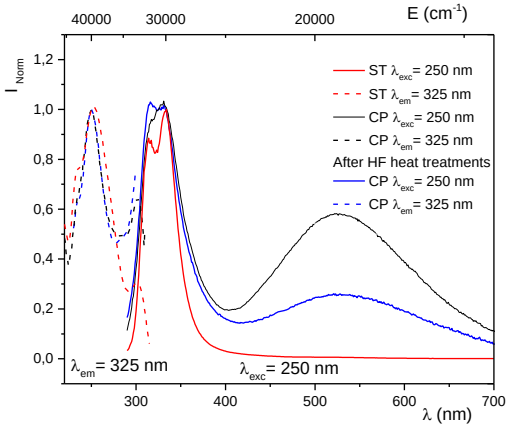

Figure SI8- Kinetic curve of the CP (a) TS (b) samples UV intensity (λ_{exc}= 250 nm; λ_{em}= 325 nm)

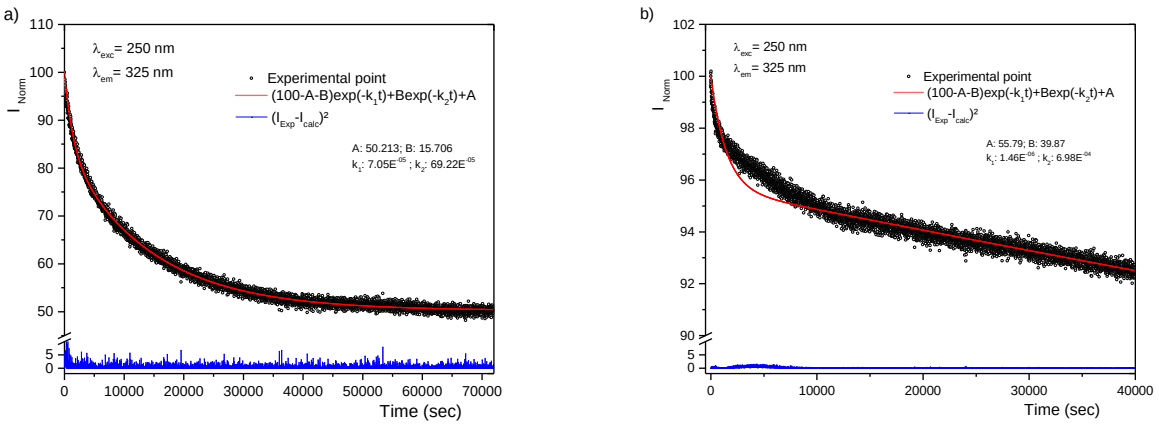

Figure SI9- Kinetic curve of UV emission of the CP before and after HT heat treatment UV intensity

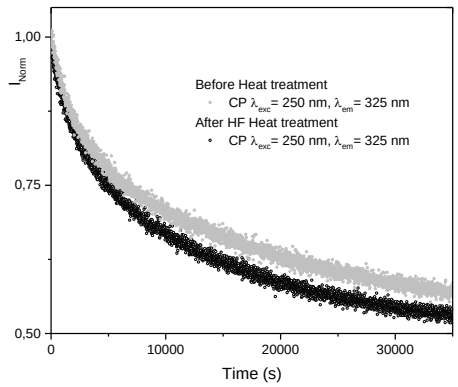

Figure SI10- Room temperature ^{119}Sn Mössbauer spectra of CP sample before and after irradiation.

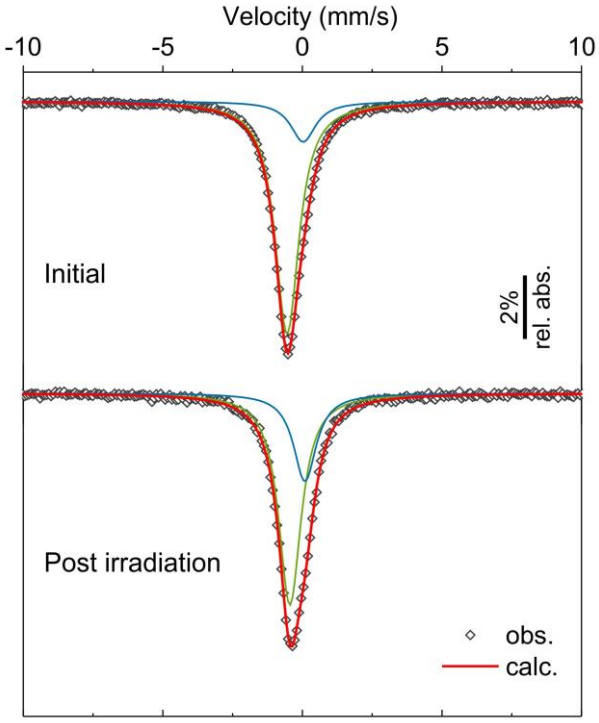

Figure SI11

Relative errors to experiment (%) of calculated values (with DFT PBE and PBEsol treatments by using a cut-off energy of 600 eV, a 11 × 11 × 11 Monkhorst-Pack k-point mesh and the force convergence set to 0.001 eV/Å) in the $CaSnF_6$ unit cell for the optimized lattice parameter, a, the unit-cell volume V and the Ca-F and Sn-F interatomic distances.

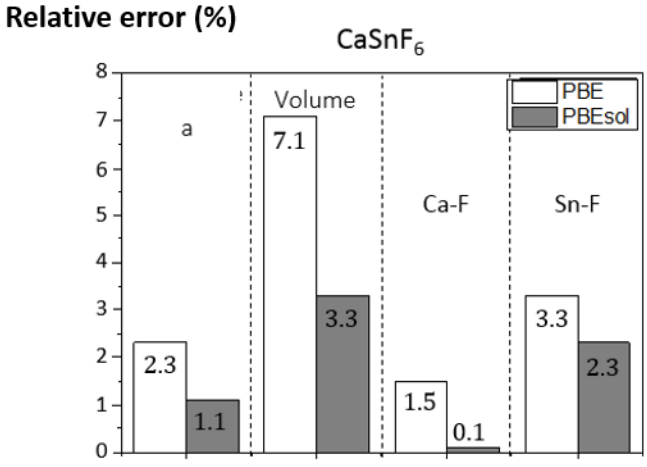

$CaSnF_6$	Exp	PBEsol	PBE
a (Å)	8,34	8,43	8,53
Δa/a (%)	/	1,1	2,3
V (Å^3)	580,30	599,73	621,65
ΔV/V (%)	/	3,3	7,1
Ca-F	2,23	2,23	2,27
Δ(Ca-F)/Ca-F (%)	/	0,1	1,5
Sn-F	1,94	1,98	2,00
Δ(Sn-F)/Sn-F (%)	/	2,3	3,3

Presentation of the various parameters for the characterization of polyhedra distortion.

Distortion index

The distortion index, D, based on bond lengths, is defined as:

$$D = \frac{1}{n}\sum_{i=1}^{n}\frac{|l_i - l_{av}|}{l_{av}}$$

where l_i are the interatomic distances (*i.e.* $d_{M\text{-}F}$ where M stands for Sn or Ce for undoped and doped matrices, respectively) from the central atom to the i^{th} coordinating atom (*i.e.* the real bond lengths), and l_{av} is the average bond length: For an octahedron, $n = 6$.

Quadratic elongation

The quadratic elongation λ is the shape unideality factor, which is calculated as:

$$\lambda = \frac{1}{n}\sum_{i=1}^{n}\left(\frac{l_i}{l_0}\right)^2$$

where l_i are the interatomic distances (*i.e.* $d_{M\text{-}F}$ where M stands for Sn or Ce for undoped and doped matrices, respectively) from the central atom to the i^{th} coordinating atom (*i.e.* the real bond lengths) and l_0 is the center-to-vertex distance of a regular polyhedron of the same volume. For an octahedron, $n = 6$.

λ is dimensionless, giving a quantitative measure of polyhedral distortion which is independent of the effective size of the polyhedron.

Bond angle variance

The bond angle variance, σ^2, is defined according to:

$$\sigma^2 = \frac{1}{m-1}\sum_{i=1}^{m}(\phi_i - \phi_0)^2$$

where m is (number of faces in the polyhedron).3/2 (*i.e.*, number of bond angles), ϕ_i is the i^{th} F-M-F bond angle, and ϕ_0 is the ideal bond angle for a regular polyhedron, with O_h symmetry, (*i.e.*, 90° for an octahedron). For an octahedron, $m = 12$.

Effective coordination number

The coordination number denotes the number of atoms coordinated to a central atom in a coordination polyhedron. It is equal to 6 for a perfectly regular octahedral coordination. Estimating the coordination of the central atom as a single number is somewhat difficult in relatively distorted coordination polyhedra. A mean or 'effective' coordination number (ECoN) can be estimated by adding all surrounding atoms with a weighting scheme, where the atoms are not counted as full atoms but as fractional atoms with numbers between 0 and 1.

$$ECoN = \sum_i w_i$$

where the quantity, w_i, called the "bond weight" of the i^{th} bond, is defined as:

$$w_i = \exp\left[1 - \left(\frac{l_i}{l_{av}}\right)^6\right]$$

In this Equation, l_{av} represents a weighted average bond length defined as:

$$l_{av} = \frac{\sum_i l_i \exp[1 - (l_i/l_{min})^6]}{\sum_i \exp[1 - (l_i/l_{min})^6]}$$

where l_{min} is the smallest bond length in the coordination polyhedron.

Table SI1- Calculated structural parameters of the 2x2x2 supercell for the undoped and Ce^{3+}-doped $CaSnF_6$ systems. Lattice constants a, b, and c given in Å (corresponding respectively to 2a', 2b' and 2c', with a', b' and c' being the lattice parameters of the $CaSnF_6$ unit cell) together with supercell volume, V, given in $Å^3$, and angles □, □ and □ given in degrees. The numbers in brackets (in %) represent the relative discrepancy with respect to the 2x2x2 undoped matrix for each calculated structural parameter

	non-doped	model i	model t	model m	model j	model p
a (Å)	16.866	17.288	16.644	16.643	16.643	16.643
		(2.50)	-(1.32)	-(1.32)	-(1.32)	-(1.32)
b (Å)	16.866	17.285	16.647	16.647	16.647	16.647
		(2.48)	-(1.30)	-(1.30)	-(1.30)	-(1.30)
c (Å)	16.866	17.285	16.647	16.647	16.647	16.647
		(2.48)	(-1.30)	(-1.30)	(-1.30)	(-1.30)
α (°)	90	89.99	90.00	90.00	90.00	90.00
		-(0.01)	(0.00)	(0.00)	(0.00)	(0.00)
β (°)	90	90.00	90.00	90.00	90.00	90.00
		(0.00)	(0.00)	(0.00)	(0.00)	(0.00)
γ (°)	90	90.00	90.00	90.00	90.00	90.00
		(0.00)	(0.00)	(0.00)	(0.00)	(0.00)
V ($Å^3$)	4797.84	5165.41	4612.10	4611.86	4611.94	4611.92
		(7.66)	(-3.87)	(-3.88)	(-3.87)	(-3.88)